Inorganic Chemistry
Article
Cite This: Inorg. Chem. XXXX, XXX, XXX−XXX
pubs.acs.org/IC

Crystal and Magnetic Structures of Melilite-Type $Ba_2MnSi_2O_7$

Matthew Sale,*[,†,‡] Qingbo Xia,[‡] Maxim Avdeev,*[,†,‡] and Chris D. Ling[‡]

[†]Australian Centre for Neutron Scattering, Australian Nuclear Science and Technology Organisation, Sydney, Australia
[‡]School of Chemistry, The University of Sydney, Sydney, Australia

Supporting Information

ABSTRACT: Melilite-type $Ba_2MnSi_2O_7$ was synthesized by a standard powder solid-state reaction route, and its magnetic properties were studied at low temperature. The magnetic structure was found to be C-type pointing along the *c* axis from neutron powder diffraction, which is different from the G-type ordering previously reported in all other 2-2-4-2 melilites with manganese as the B′-site transition metal. Ab initio (density functional theory) and magnetic dipole−dipole calculations were used to understand the magnetic structure by determining the spin supersuperexchange parameters as well as the relative influence of spin−orbit coupling and the magnetic dipole−dipole interactions.

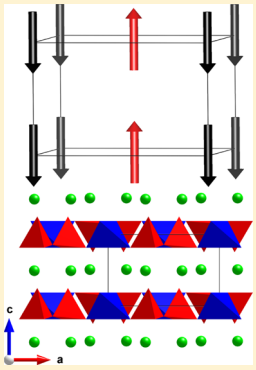

INTRODUCTION

Many oxides of the general formula $A_2B'C''_2O_7$ adopt the melilite-type crystal structure (where *A* = alkali, alkali-earth, rare-earth cations, larger *B*′ = Al, Be, Ga, Ge, Mg, Si, transition metal, and smaller *C*″ = Al, Be, Ga, Ge, P, Si, V).[2] The melilite series is exemplified by the solid solution between åkermanite ($Ca_2MgSi_2O_7$) and gehlenite ($Ca_2Al_2SiO_7$).[3,4]

The melilite-type structure is built of layers of vertex-sharing $B'O_4$ and $C''O_4$ tetrahedra separated by alkali-metal atoms *A* residing in the interlayer space (Figure 1). It is described by the noncentrosymmetric tetragonal space group $P4\bar{2}_1m$ (No. 113) with unit cell parameters in the range $a = b \approx 7.3-8.6$ Å and $c \approx 4.8-5.6$ Å.[2] Many melilites form an incommensurate phase at lower temperatures due to a "misfit between the intermediate cation layer and the sheet-like tetrahedral framework".[2,5]

The *B*′-site of the melilite structure can accommodate many different transition-metal elements, including manganese, cobalt, copper, and iron, which possess net magnetic moments due to their unpaired d electrons and orbital angular momentum. The primary magnetic interaction between *B*′-site transition-metal atoms in melilites is the relatively strong antiferromagnetic (AFM) intralayer supersuperexchange (SSE) interaction[6−8] which operates through the $C''O_4$ tetrahedra (J_1 in Figure 2). As a result, these materials usually exhibit either a G-type or C-type AFM magnetic ordering.[7,9] Depending on composition, spin−orbit coupling (SOC) can also be quite strong.[10,11]

These materials have attracted substantial interest for studying the dynamics of 2-D quantum mechanical systems[8] due to the relatively weak interlayer interactions along [001] and the convenience of magnetic phase transitions at experimentally accessible magnetic fields.[12,13] The two-dimensional character of the magnetic sublattice leads to a variety of magnetic structures such as long-range commensurate ($Ba_2MnGe_2O_7$,[14] $Sr_2CoGe_2O_7$[9]) or incommensurate ($Ba_2CuGe_2O_7$[15]) magnetic ordering. Furthermore, many melilites exhibit multiferroic ordering due to the noncentrosymmetric space group[16,17] which is observable in both static ferroelectric and terahertz optical absorption measurements.[18−20] The p−d hybridization mechanism is usually responsible for this coupling between magnetic moments and ferroelectric polarization.[20,21]

Various compositions in the 2-2-4-2 magnetic melilite group with manganese on the *B*′-site[22,23] have been previously synthesized, including $Sr_2MnSi_2O_7$,[5,23−34] $Ba_2MnSi_2O_7$,[23−25,28] $Sr_2MnGe_2O_7$,[9,25,28,35−38] and $Ba_2MnGe_2O_7$.[6,14,20,21,32,39−42] $Eu_2MnSi_2O_7$[31] and $Sr_2MnGe_2(S_6O)$[43] were also synthesized and characterized magnetically but have somewhat different magnetic properties due to the presence of the additional magnetic Eu ion and the much stronger interatomic bonding from the S ions. Mn can also be accommodated on the *B*′-site in a solid solution with other *B*′-site ions.[27,38,40] Previous attempts to synthesize pure $Ca_2MnSi_2O_7$ and $Ca_2MnGe_2O_7$ melilite compounds were unsuccessful.[23,44−49] However, Ca can still be accommodated on the *A*-site in the melilite manganese structure with solid solution partial substitution of the *A*-site[44,45] and/or also the *B*′-site.[5,23,50,51]

Manganese in the 2+ oxidation state has a magnetic moment from the combined spin of its five unpaired d electrons. Previous measurements including magnetometry, neutron powder diffraction (NPD), inelastic neutron scattering (INS), and density functional theory (DFT) calculations all

Received: November 15, 2018

DOI: 10.1021/acs.inorgchem.8b03195
Inorg. Chem. XXXX, XXX, XXX−XXX

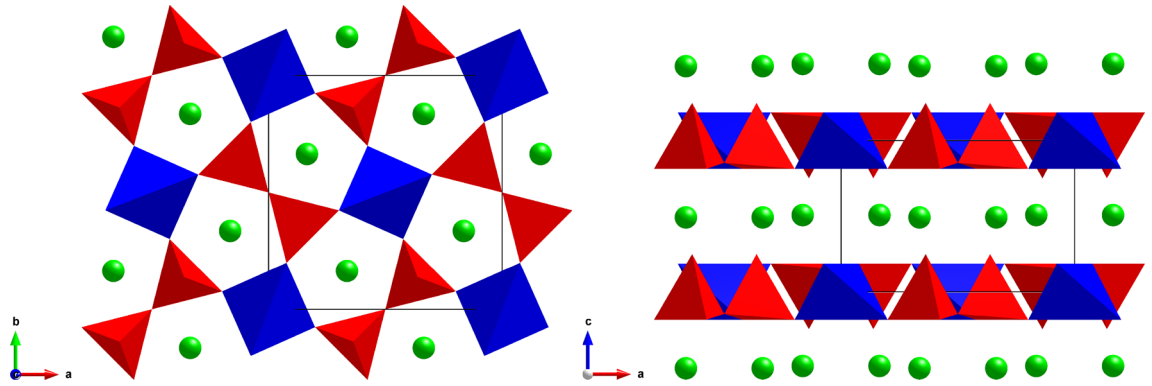

Figure 1. Melilite structure ($Ba_2MnSi_2O_7$ at 50 K; $P42_1m$ (No. 113))[1]

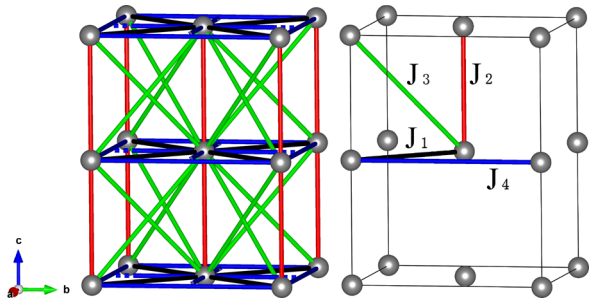

Figure 2. Different SSE pathways which were examined using DFT. Color scheme: black, J_1; red, J_2; green, J_3; blue, J_4.

suggest a G-type magnetic structure for $Sr_2MnSi_2O_7$,[32−34] $Sr_2MnGe_2O_7$,[9,37] $Ba_2MnGe_2O_7$,[14,21,32] and $Sr_2MnGe_2(S_6O)$.[43] The contribution from SOC for the tetrahedrally coordinated Mn in a 2+ state is nearly negligible.[52] Some crystal-field splitting may be possible in melilite materials, as the tetrahedrally coordinated metal atoms are slightly compressed along the *c* axis. Previous measurements and calculations of SOC and single ion anisotropy (SIA) values for manganese melilites have shown these values to be quite small.[20,32,37] SIA has been observed in microwave transmission experiments of 0.023(6) K in $Ba_2MnGe_2O_7$,[20] which is about twice as large as the interlayer SSE of 0.012(1) K for the same material measured with INS[14] (although these two values were not refined synchronously). As a result, magnetic dipole−dipole interactions, which are always present but are usually insignificant in comparison to other magnetic interactions, can have a significant effect on the direction of the magnetic moments.[32,37]

$Ba_2MnSi_2O_7$ was first prepared and identified as melilite type on the basis of indexing of X-ray powder diffraction data.[23] The unit cell parameters and melilite crystal structure type were later confirmed,[24,53] but a detailed crystal structural study was not carried out. Analysis of the bond geometry of a wide class of melilites in the 2-2-4-2 group was performed, but the ionic positions were only described by equations relating to the space group and the trends of the unit cell parameters.[24] Distortion of the transition-metal tetrahedra was also speculated in this paper.[24] Raman and infrared spectra of $Ba_2MnSi_2O_7$ and related compounds in the 2-2-4-2 melilite structure and other unspecified crystal structure types were also studied.[25] Existing information about $Ba_2MnSi_2O_7$ as well as many other materials was used as input for a machine-learning algorithm to predict the properties of many materials.[28]

Finally, while the magnetic properties and structure of other manganese melilites have been reasonably well studied, there appears to be no literature on the magnetic properties and magnetic structure of $Ba_2MnSi_2O_7$. In contrast to all other materials in this group, our DFT calculations predict that $Ba_2MnSi_2O_7$ has a C-type magnetic structure. Therefore, we performed further research on melilite $Ba_2MnSi_2O_7$ to study its ionic structure, magnetic structure, and magnetic properties. Here, we report the results of powder sample synthesis, X-ray powder diffraction, magnetometry, neutron powder diffraction (NPD), ab initio DFT calculations with spin−orbit coupling (SOC) calculations, and magnetic dipole−dipole (MDD) calculations for $Ba_2MnSi_2O_7$.

EXPERIMENTAL SECTION

Materials Synthesis. A powder sample of $Ba_2MnSi_2O_7$ was synthesized by a solid-state reaction. Stoichiometric amounts of $BaCO_3$ (99.98%, Aldrich), $MnCO_3$ (>98.0%, BDH), and SiO_2 (99.98%, Aldrich) were mixed and milled on a planetary ball mill at 360 rpm for 2 h using a small quantity of acetone as the dispersant. After drying, the well-mixed reactants were placed into an open alumina crucible and calcined at 900 °C for 10 h to decompose the carbonates, following by an intermediate grinding. The final product $Ba_2MnSi_2O_7$ was obtained by sintering the product collected in the last step at 1200 °C for 20 h. The powder had a light brown appearance.

X-ray Analysis. Progress of the synthesis was monitored by collecting XRPD data on a Panalytical X'Pert Pro diffractometer. Sintering was repeated until XRPD data of the sample did not change between successive treatments. The majority of the strongest peaks in the XRPD pattern for the final product matched well with the standard XRPD pattern[53] of melilite-type $Ba_2MnSi_2O_7$. XRPD and NPD also showed the presence of a glaserite-type $Ba_3MnSi_2O_8$ impurity phase (14.3 wt %), which we could not eliminate by varying the experimental synthesis conditions. The glaserite phase crystal structure was reported recently and does not order magnetically above 1.6 K, which is the lowest temperature reached in this experiment.[54] Mn_3O_4 was also found to be present at the level of 3.6 wt % from NPD.

dc Magnetic Susceptibility and Heat Capacity. Magnetometry data were collected on a Quantum Design 9T Physical Properties Measurement System (PPMS) with the vibrating sample magnetometer (VSM) option. For the zero field-cooled (ZFC) and field-cooled (FC) temperature-dependent magnetic susceptibility measurements from 3 to 300 K, a 500 Oe magnetic field was used with a VSM oscillation frequency of 40 Hz, an amplitude of 2 mm and an averaging time of 2 s. The magnetic susceptibility was fitted to the modified Curie−Weiss law $\chi_{exp} = C/(T - \Theta) + \chi_T$, where C is the Curie constant, Θ is the Curie−Weiss temperature, and χ_T is the temperature-independent paramagnetic contribution. The

DOI: 10.1021/acs.inorgchem.8b03195
Inorg. Chem. XXXX, XXX, XXX−XXX

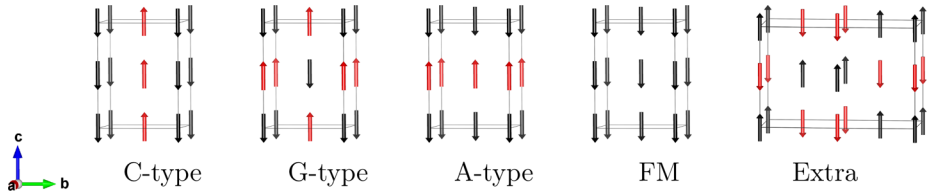

Figure 3. Different magnetic configurations used to perform DFT magnetic energy calculations to determine spin-exchange calculations and mean field Curie–Weiss temperature.

$Ba_3MnSi_2O_8$ glaserite and Mn_3O_4 impurities were represented as a proportion of the molar mass in the analysis.

A more detailed measurement of magnetic susceptibility was also performed over a small low-temperature interval from 2 to 6 K to more accurately determine the Néel temperature of the magnetic phase transition of $Ba_2MnSi_2O_7$. For these measurements, a 1000 Oe magnetic field was used with a VSM oscillation frequency of 40 Hz and amplitude of 0.5 mm. The temperature was stabilized at intervals of 0.05 K with a 60 s pause after temperature stabilization, where 20 separate measurements were performed with 2 s averaging to obtain more accurate data. A smoothing filter similar to a Savitzky–Golay filter[55] was applied to the data by fitting a fourth-order polynomial over an interval of 0.5 K, which also generates an approximation to the derivatives. Specific heat measurements were performed on the same type of platform over a similar temperature range.

Magnetic field hysteresis was performed at 2.5, 25, and 50 K to help identify the ferrimagnetic contribution from the small amount of Mn_3O_4 impurity found in the sample which is clearly visible in both the FC and ZFC magnetometry measurements. These hysteresis measurements were taken from −9 to 9 T with an oscillation frequency of 40 Hz, amplitude of 2 mm, and averaging time of 2 s.

Neutron Analysis. Neutron powder diffraction (NPD) patterns were collected on the high-resolution powder diffractometer Echidna[56] at the OPAL facility (Lucas Heights, Australia) using neutrons of wavelength 2.4395 Å. Approximately 2 g of the powder sample was loaded in a 6 mm diameter cylindrical vanadium can, and diffraction patterns were collected at 1.6 and 50 K using a helium cryostat. The magnetic structure was analyzed using the FullProf suite[57] with the default neutron scattering lengths and Mn^{+2} magnetic form factor.

Theoretical Analysis. For our ab initio DFT calculations, we employed the Vienna ab initio simulation package (VASP, version 5.2.12[58−61]) in the generalized gradient approximation (GGA) of Perdew, Burke, and Ernzerhof[62] with the projector augmented-wave (PAW) method.[63,64] A Γ-centered 3 × 3 × 3 Monkhorst–Pack *k*-point mesh[65] with the Gaussian smearing method[66] was used for the calculations with a plane wave energy cutoff of 500 eV. Additional settings to improve electronic stability are outlined in the input files provided in the Supporting Information. All calculations were performed as spin-polarized calculations, and the GGA + onsite repulsion (GGA+U) method was used to correct the well-known overbinding of electrons in the 3d metal atoms of manganese[67] with $U-J$ = 5 eV (unless otherwise stated), which is a commonly used value.[37,68−70]

The melilite crystal structure[31] was represented by a 1 × 1 × 2 supercell unless otherwise stated, which is large enough to represent the G-type and A-type magnetic configurations (Figure 3). Ionic relaxation was performed to obtain an appropriate crystal structure before further magnetic calculations. In all ionic relaxations, no symmetry was imposed on the ionic positions and the unit cell parameters were allowed to vary freely. Ionic relaxations were restarted several times to eliminate the effects of Pulay stress.[71]

Spin supersuperexchange (SSE) energies and the calculation of the Curie–Weiss temperature in the mean field approximation were determined using the energy mapping method as for previous calculations.[32,37,72] The bond lengths, bond angles, and dihedral angles of the atoms between Mn sites were examined to identify symmetry-inequivalent bond chains as different possible SSE pathways (Figure 2). The energy of the G-type, C-type, and A-type antiferromagnetic (AFM) and ferromagnetic (FM) magnetic structures (Figure 3) were calculated with $U-J$ values of 4, 5, and 6 eV as the calculated energies, and spin-exchange values are affected by this setting.[32,37,67,72−74] These calculations were performed with fixed ionic positions using the final structure relaxed with the C-type magnetic structure from the previous step. From these energy values, the J_1, J_2, and J_3 SSE constants were calculated using a method similar to that in our previous work[75] and the interaction matrices in Table 1.

Table 1. Spin-Exchange Matrices and Bond Counts for the (Top) 1 × 1 × 2 and (Bottom) 1 × 2 × 2 Supercells for Input Energy per Formula Unit (fu)

$$M = \begin{array}{c} \\ FM \\ A-type \\ C-type \\ G-type \end{array} \begin{array}{c} \begin{array}{cccc} Constant & J_1 & J_2 & J_3 \end{array} \\ \begin{pmatrix} 1 & 2 & 1 & 4 \\ 1 & 2 & -1 & -4 \\ 1 & -2 & 1 & -4 \\ 1 & -2 & -1 & 4 \end{pmatrix} \end{array}$$

$$M = \begin{array}{c} \\ Bond\ Counts \end{array} \begin{array}{c} \begin{array}{cccc} Constant & J_1 & J_2 & J_3 \end{array} \\ \begin{pmatrix} 0 & 4 & 2 & 8 \end{pmatrix} \end{array}$$

$$M = \begin{array}{c} \\ FM \\ A-type \\ C-type \\ G-type \\ Extra \end{array} \begin{array}{c} \begin{array}{ccccc} Constant & J_1 & J_2 & J_3 & J_4 \end{array} \\ \begin{pmatrix} 1 & 2 & 1 & 4 & 4 \\ 1 & 2 & -1 & -4 & 4 \\ 1 & -2 & 1 & -4 & 4 \\ 1 & -2 & -1 & 4 & 4 \\ 1 & 0 & -1 & 0 & 0 \end{pmatrix} \end{array}$$

$$M = \begin{array}{c} \\ Bond\ Counts \end{array} \begin{array}{c} \begin{array}{ccccc} Constant & J_1 & J_2 & J_3 & J_4 \end{array} \\ \begin{pmatrix} 0 & 4 & 2 & 8 & 4 \end{pmatrix} \end{array}$$

Further calculations with a larger 1 × 2 × 2 supercell and the addition of an extra spin configuration also allowed us to calculate the strength of the J_4 interaction for $U-J$ = 5 eV. From these spin-exchange values, the mean-field approximation to the Curie–Weiss intercept temperature was also calculated (Table 5).

DFT SOC and MDD[76] calculations were performed with fixed ionic positions, and both C-type and G-type magnetic structures with moments aligned along [100], [110], [010], and [001]. For the DFT SOC calculations the charge density was also allowed to vary self-consistently. To determine the total energy of the MDD interactions, the MDD energy was summed over a large supercell up to 250 Å. As MDD calculations are not strongly convergent and are sensitive to stray magnetic dipoles, even at large distances, a parallelepiped supercell boundary condition centered on the atom being calculated combined with the symmetry of the melilite structure ensured a symmetric contribution to the total energy from each magnetic dipole; the Ewald summation method was not employed.[77,78] We summed together the contribution of both SOC and MDD to evaluate the preferred magnetic direction and ground-state magnetic structure.

DOI: 10.1021/acs.inorgchem.8b03195
Inorg. Chem. XXXX, XXX, XXX−XXX

RESULTS

Magnetometry and Heat Capacity. The high-temperature ZFC and FC magnetic susceptibility data from 250 to 295 K were analyzed to determine the Curie–Weiss intercept temperature and magnetic moment of the Mn atoms (Figure 4

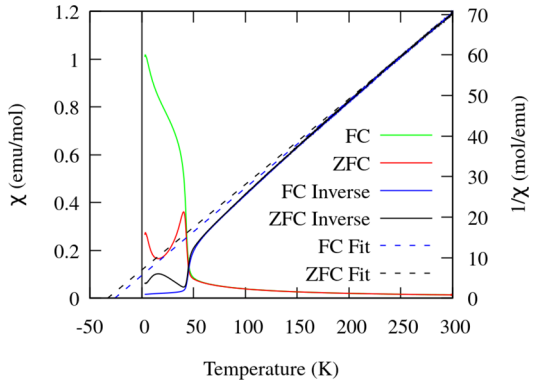

Figure 4. Zero field-cooled and field-cooled magnetic susceptibility and inverse magnetic susceptibility with fitted Curie–Weiss linear function of the mixed $Ba_2MnSi_2O_7$ melilite (82.1 wt %) $Ba_3MnSi_2O_8$, glaserite (14.3 wt %), and Mn_3O_4 (3.6 wt %). While the glaserite sample does not order magnetically at the temperatures in this measurement, the Mn_3O_4 impurity produced a large amount of ferrimagnetic signal which is clearly visible with a peak at around 33–41 K.[79]

Table 2. Fitted Curie–Weiss Parameters from Magnetic Susceptibility Measurements over the 250–295 K Temperature Interval

field cooling	Curie–Weiss constant	magnetic moment (μ_B)	Curie–Weiss intercept (K)
zero field	4.74(1)	6.16(1)	−33.0(5)
field	4.64(1)	6.09(1)	−26.1(4)
ideal[80,81]		5.92	

and Table 2) in our melilite powder sample with some impurities. The negative Curie–Weiss intercept suggests predominant AFM interactions in the sample. The Curie–Weiss fitted magnetic moment is also very close to the ideal value for Mn^{2+} in a high-spin state of 5.92 μ_B.

At lower temperatures, two magnetic ordering peaks are observed in the magnetic susceptibility. The 33–41 K peak corresponds to the magnetic ordering temperature of the ferrimagnetic Mn_3O_4 impurity.[79] The magnetometry peak observed at around 3 K is associated with the onset of magnetic ordering of the melilite phase. The glaserite phase does not show any magnetic ordering down to 1.6 K from previous neutron and magnetometry experiments[54] and therefore does not contribute to this magnetometry peak. While the small amount of ferrimagnetic Mn_3O_4 makes a significant ferrimagnetic contribution to the magnetic susceptibility plots at low temperatures, it should affect only a small percentage of the Curie–Weiss fitted magnetic moment due to the small weight percentage.

Magnetic hysteresis measurements at 2.5, 25, and 50 K were performed to further investigate the observed ferrimagnetic signal in our sample. As can be seen in Figure 5, a FM ordering is observed at both 2.5 and 25 K, which we assign to the

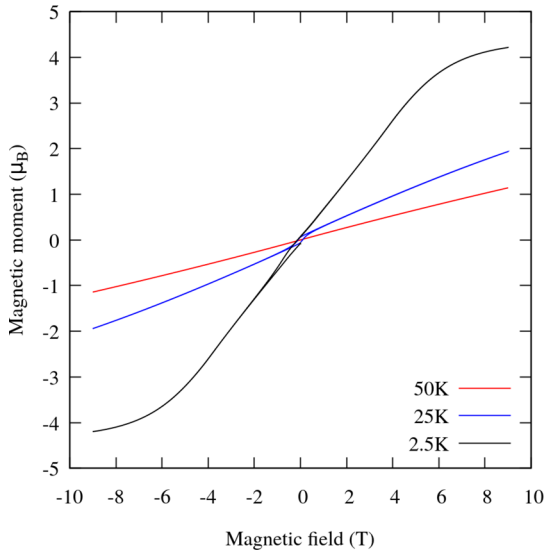

Figure 5. Magnetic field hysteresis at 2.5, 25, and 50 K for the mixed $Ba_2MnSi_2O_7$ melilite (82.1 wt %), $Ba_3MnSi_2O_8$ glaserite (14.3 wt %), and Mn_3O_4 (3.6 wt %) powder sample. The ferrimagnetic ordering of the Mn_3O_4 impurity is seen in the 25 and 2.5 K measurements but not in the 50 K measurement. Saturation of the magnetic moments is mostly achieved at 2.5 K and 9 T magnetic field, which is the maximum field achievable by our instrumentation.

ferrimagnetic ordering of Mn_3O_4. No significant increase in FM ordering was observed in the 2.5 K hysteresis, but the ferrimagnetic ordering of Mn_3O_4 masks any observation of a small FM canting of $Ba_2MnSi_2O_7$ if it existed.

The Néel temperature was determined to be about 2.95 K from the intercept of the second derivative of the temperature-dependent magnetic susceptibility and the peak in the heat capacity data (Figure 6[82−87]).

Neutron Powder Diffraction (NPD). The crystal structure of $Ba_2MnSi_2O_7$ was refined from NPD data collected at 50 K: i.e. in the paramagnetic range. The refinement confirmed that the composition crystallized in the melilite structure type (space group $P4\bar{2}_1m$, No. 113). Contributions from the Mn_3O_4 and glaserite $Ba_3MnSi_2O_7$[54] impurities were accounted for in the refinement. The refined crystal structural parameters are given in Table 3, and the Rietveld plot is presented in Figure 7.

The NPD pattern taken at 1.6 K showed additional peaks due to the magnetic ordering. All the magnetic peaks could be indexed by the chemical unit cell, i.e. with the propagation vector k = (0,0,0). $Ba_3MnSi_2O_8$ was found to be paramagnetic down to the lowest experimentally achievable temperature of 1.6 K from previous studies[54] and thus does not present any extra neutron diffraction peaks at these temperatures. Representational analysis performed with BasIreps for the Mn atoms located in the 2a (0, 0, 0) site followed by model testing unambiguously pointed to the irreducible representation Γ1 with a single basis vector. The model, also equivalent to the magnetic space group $P4\bar{2}_1m$ (Opechowski–Guccione[88] #113.1.929), corresponds to the magnetic structure in which Mn magnetic moments form the so-called C-type structure and are aligned along the c axis. The value of the magnetic moment at 1.6 K was refined to 4.1(1) μ_B. Assuming Brillouin function behavior of the magnetization and transition temperature at 3 K (Figure 6), this corresponds to a saturated magnetic moment of 4.7(1) μ_B, close to the expected value for the

DOI: 10.1021/acs.inorgchem.8b03195
Inorg. Chem. XXXX, XXX, XXX−XXX

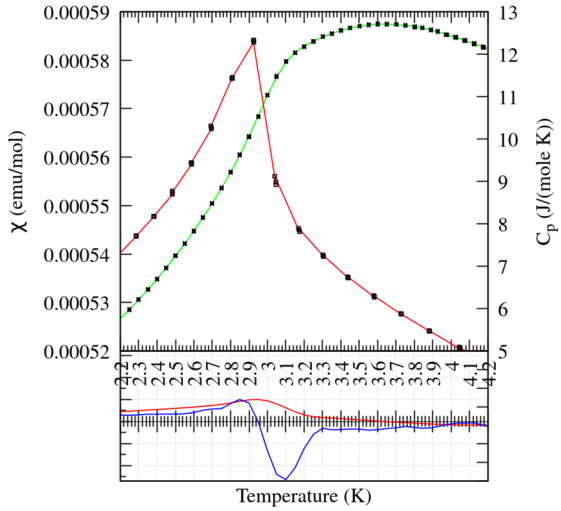

Figure 6. (top left, green) Zero field-cooled magnetic susceptibility under 1000 Oe magnetic field and smoothed with a fourth-order polynomial least-squares regression over a 0.5 K interval (which produces smoothing and derivatives similar to a Savitzky–Golay filter[55]) of the mixed $Ba_2MnSi_2O_7$ melilite (82.1 wt %), $Ba_3MnSi_2O_8$ glaserite (14.3 wt %), and Mn_3O_4 (3.6 wt %) sample. (top right, red) Heat capacity data $C_p(T)$. (bottom) First and second derivatives of the smoothed magnetic susceptibility as red and blue, respectively (arbitrary scale). The second-derivative intercept of magnetic susceptibility is at the same value as the heat capacity peak within experimental error.

S = 5/2 Mn^{+2} ion. The Rietveld plot for the NPD data collected at 1.6 K is presented in Figure 7.

From the refined structure, the distortion of the MnO_4 tetrahedron was characterized. The quadratic elongation is 1.0213 and bond angle variance is 77.4724, while the O–Mn–O angles along the c direction are 104.01(9)° and in the a–b plane are 121.05(9)°.[1,89] This shows that there is some compression of the tetrahedra along the c axis which may produce some crystal-field splitting.[90,91]

DFT Ionic Relaxation. DFT calculations were performed to investigate the magnetic structure of melilite $Ba_2MnSi_2O_7$. This structure was ionically relaxed in both a G-type and C-type magnetic structure. Even though no symmetry was imposed on the degrees of freedom of the atomic positions, the final symmetry was still the same as the original symmetry space group to better than 10^{-5} Å. The ionic relaxation with the C-type magnetic structure was found to have the lowest structural energy by 0.150 K/fu. Example calculation input files and final relaxed structures can be found in the Supporting Information.

DFT Magnetic Energies and Spin Supersuperexchange Constants. Further spin-polarized DFT calculations with fixed atom positions using the C-type ionically relaxed structure were performed to determine the magnetic spin SSE interaction constants and the calculated Curie–Weiss temperature. The G-type or C-type AFM ordering of melilites is usually caused by the relatively strong AFM ordering between metal atoms in the a–b plane which is mediated by the intralayer spin SSE, labeled as J_1 in Figure 2. The sign of the intralayer spin SSE between a–b plane layers determines if the magnetic structure is G type or C type. Two other spin SSE pathways allowed by symmetry were also evaluated in our calculations but are expected to be relatively weak.

As can be seen in Table 5, these calculations also predict a C-type AFM magnetic structure from both the total energies and the spin-exchange energies. A value of U–J = 5 eV is similar to the ideal value for similar calculations found in the literature[37,68] and gives good agreement between our own experimental magnetometry measurements and calculations of the Curie–Weiss temperature. The J_1 spin-exchange pathway is about 30 times greater than for J_2 at U–J = 5 eV, which shows that this material is a reasonably good approximation to a 2-D magnetic system. The J_3 and J_4 longer pathways have little effect on the magnetic structure, as they are relatively weak in comparison to their direct competitors J_2 and J_1, respectively. However, they may still be observable, for example, by INS or terahertz spectroscopy.

Magnetic Dipole–Dipole (MDD) Calculations and DFT Spin–Orbit Coupling (SOC). After measuring the direction of the magnetic moments along the c axis using NPD, we performed self-consistent DFT SOC calculations and MDD to investigate the preferred ground-state magnetic moment directions (Table 6). Both a C-type and G-type magnetic structure were evaluated, as the energies calculated are similar to the J_2 spin-exchange energy and may therefore affect the calculated magnetic ground state. While the DFT SOC calculations show a preferred moment direction in the a–b plane, the influence of MDD is stronger and puts the moments along the c axis by 0.0578(41) K at U–J = 5 eV, as measured in our NPD experiment. Also, evaluation of the G-type magnetic structure total energy is still higher for all magnetic moment directions than in the C-type structure. Evaluating only the effect of SOC gives a Λ term of about 0.3082(41) K at U–J = 5 eV, which is about 1 order of magnitude larger than 0.023(2) K for $Ba_2MnGe_2O_7$.[20] We assume that this SOC is due to the distortion of the MnO_4 tetrahedra. While the chosen U–J value has some influence on the final value, moments pointing along the c axis in the C-type magnetic structure is still the preferred direction for all U–J values. It should be noted that the calculated DFT SOC energy differences are very small and may therefore be limited in overall accuracy. Therefore, we can write the following magnetic Hamiltonian for melilite $Ba_2MnSi_2O_7$ from the SSE, SOC, and MDD terms on the

Table 3. Refined Crystal Structure Parameters for $Ba_2MnSi_2O_7$ Based on NPD Data Collected at 50 K[a]

atom	site	x	y	z	U_{iso}, Å^2
Ba	4e (x, 1/2 + x, z)	0.1644(2)	0.6644(2)	0.5076(5)	0.0016(8)
Mn	2a (0, 0, 0)	0	0	0	0.0031(16)
Si	4e (x, 1/2 + x, z)	0.6327(3)	0.1327(3)	0.9462(7)	0.0089(5)
O1	2c (0, 1/2, z)	0	1/2	0.1466(7)	0.0089(5)
O2	8f (x, y, z)	0.0764(2)	0.1989(2)	0.1864(4)	0.0089(5)
O3	4e (x, 1/2 + x, z)	0.6378(2)	0.1378(2)	0.2493(5)	0.0089(5)

[a]Space group $P42_1m$ (No. 113), a = 8.32075(18) Å, c = 5.37185(13) Å, V = 371.919(15) Å^3.

DOI: 10.1021/acs.inorgchem.8b03195
Inorg. Chem. XXXX, XXX, XXX–XXX

Table 4. Refined Crystal Structure Parameters for $Ba_2MnSi_2O_7$ Based on NPD Data Collected at 1.6 K[a]

atom	site	x	y	z	U_{iso}, Å^2
Ba	4e (x, 1/2 + x, z)	0.1649(2)	0.6649(2)	0.5086(5)	0.0040(7)
Mn	2a (0, 0, 0)	0.00000	0.00000	0.00000	0.0128(15)
Si	4e (x, 1/2 + x, z)	0.6342(3)	0.1342(3)	0.9486(6)	0.0088(4)
O1	2c (0, 1/2, z)	0.00000	0.50000	0.1441(6)	0.0088(4)
O2	8f (x, y, z)	0.07745(16)	0.19903(16)	0.1872(3)	0.0088(4)
O3	4e (x, 1/2 + x, z)	0.63828(19)	0.13828(19)	0.2508(4)	0.0088(4)

[a]Space group $P42_1m$ (No. 113), a = 8.32046(7) Å, c = 5.37097(5) Å, V = 371.832(6) Å^3.

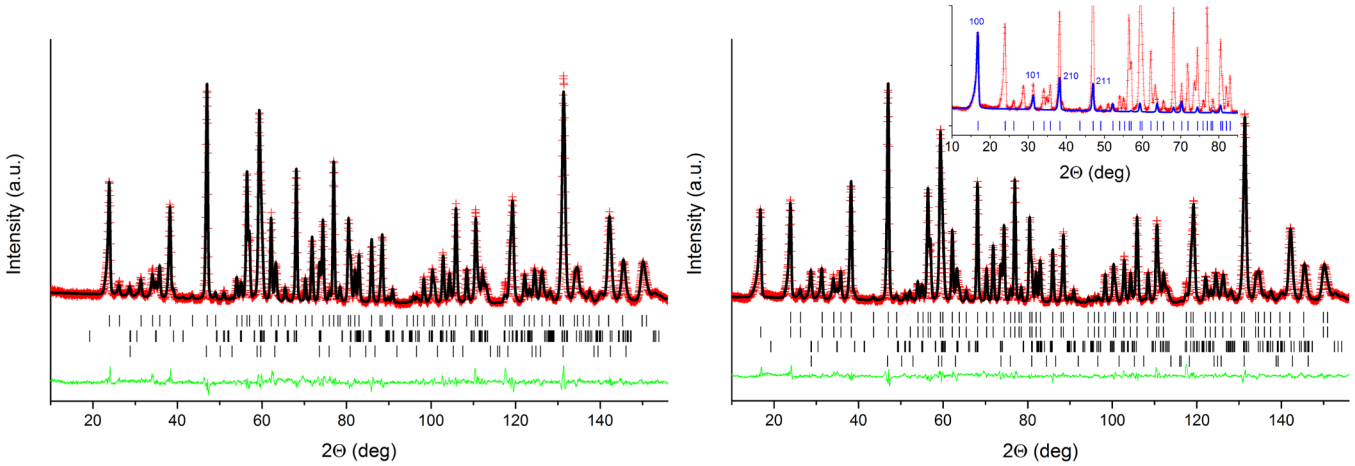

Figure 7. (left) Rietveld plot for the NPD data collected at 50 K (λ = 2.4395 Å). R_p = 4.12%, R_{wp} = 5.78%. Red crosses and black and green solid lines are experimental and calculated data and their difference, respectively. The tick marks from top to bottom show peak positions for 82.1 wt % of $Ba_2MnSi_2O_7$, 14.2 wt % of $Ba_3MnSi_2O_8$, and 3.7 wt % Mn_3O_4, respectively. (right) Rietveld plot for the NPD data collected at 1.6 K. R_p = 3.61%, R_{wp} = 5.04%, R_{mag} = 4.95%. The tick marks from top to bottom show peak positions for $Ba_2MnSi_2O_7$, $Ba_2MnSi_2O_7$ magnetic, $Ba_3MnSi_2O_8$, and 3.7 wt % Mn_3O_4, respectively. The inset with the blue curve shows the magnetic contribution.

Table 5. Magnetic Energies Calculated with DFT in Different Spin Configurations as well as Calculated Spin-Exchange Constants and the Mean-Field Approximation to the Curie−Weiss Temperature at Various $U-J$ Values for the C-Type Relaxed Melilite Structure[a]

	$U-J$ value (eV)			
	4	5	5 (larger unit cell)	6
C-type (K/fu)	0.000000(29)	0.000000(29)	0.000000(14)	0.000000(29)
G-type (K/fu)	0.202839(29)	0.149828(29)	0.149622(14)	0.108096(29)
FM (K/fu)	10.640012(29)	6.829635(29)	6.824900(14)	4.058280(29)
A-type (K/fu)	10.713527(29)	6.914560(29)	6.909860(14)	4.145927(29)
extra type (K/fu)			3.407231(14)	
J_1 (K)	−0.4230140(18)	−0.2718873(18)	−0.2717028(10)	−0.1619222(18)
J_2 (K)	0.0110541(36)	0.0093901(36)	0.0093833(20)	0.0078297(36)
J_3 (K)	−0.00129324(91)	−0.00064903(91)	−0.00064662(49)	−0.00020448(91)
J_4 (K)			−0.0049004(12)	
Θ (K)	−4.900857(37)	−3.132387(37)	−3.187389(21)	−1.848190(37)

[a]Errors refer to numerical noise in calculations.

basis of interpretation of experimental and DFT calculation results.

$$H = \mathrm{SSE} + \mathrm{SOC} + \mathrm{MDD}$$
$$= -\sum_{i<j,m} J_m \mathbf{S}_i \cdot \mathbf{S}_j + \sum_i \Lambda (S_i^z)^2 + \sum_{i<j} \left(\frac{g^2 \mu_B^2}{a_0^3}\right)\left(\frac{a_0^3}{r_{ij}^3}\right)$$
$$[-3(\bar{S}_i \cdot \hat{r}_{ij})(\bar{S}_j \cdot \hat{r}_{ij}) + (\bar{S}_i \cdot \bar{S}_j)]$$

Where i and j are atom indices, J_m are the spin-exchange constants/pathways, Λ is the SIA not including that contributed by MDD, g = 2, a_0^3 = 0.529177 Å (the Bohr radius), μ_B is the Bohr magneton, and $\frac{(g\mu_B)^2}{a_0^3}$ = 8.409 K.[76] For $U-J$ = 5 eV, our DFT calculations give J_1 = −0.272, J_2 = 0.00938, J_3 = −0.000647, J_4 = 0.00490, and Λ = −0.308 (in units of K).

CONCLUSIONS

The $Ba_2MnSi_2O_7$ melilite structure with space group $P42_1m$ (No. 113) was confirmed with NPD. Magnetometry of our melilite powder sample with impurities gives predominant AFM interactions in this material with a negative Curie−Weiss temperature of −33.0(5) K and effective magnetic moment of

DOI: 10.1021/acs.inorgchem.8b03195
Inorg. Chem. XXXX, XXX, XXX−XXX

Table 6. Results of Self-Consistent DFT SOC and MDD Calculations with Various Magnetic Moment Directions and Magnetic Structures[a]

			$U-J$ value (eV)					
			SOC			total		
magnetic structure	moment direction	MDD	4	5	6	4	5	6
C type	[100]	0.1222(1)	0.0000(29)	0.0000(29)	0.0001(29)	0.1222(29)	0.1222(29)	0.1223(29)
	[110]	0.1222(1)	0.0015(29)	0.0069(150)	0.0010(29)	0.1237(29)	0.1290(150)	0.1232(29)
	[010]	0.1222(1)	0.0009(29)	0.0004(40)	0.0000(29)	0.1231(29)	0.1226(40)	0.1222(29)
	[001]	−0.2443(1)	0.3258(29)	0.3087(29)	0.2961(29)	0.0815(29)	0.0644(29)	0.0518(29)
G type	[100]	−0.0232(2)	0.2213(29)	0.1622(29)	0.1206(29)	0.1982(29)	0.1390(29)	0.0975(29)
	[110]	−0.0232(2)	0.2221(29)	0.1625(29)	0.1214(29)	0.1990(29)	0.1394(29)	0.0983(29)
	[010]	−0.0232(2)	0.2213(29)	0.1692(150)	0.1228(29)	0.1981(29)	0.1461(150)	0.0996(29)
	[001]	0.0463(2)	0.5467(29)	0.4755(29)	0.4185(29)	0.5931(29)	0.5219(29)	0.4648(29)

[a]Energy in K/fu. DFT SOC energy values have been shifted by the lowest energy value per different type of $(U-J)$ value.

6.16(1) μ_B (ZFC), which is close to the ideal value for Mn^{2+} of 5.92 μ_B. NPD gives a C-type collinear magnetic structure with moments pointing along the c axis and magnetic moment extrapolated to 0 K of 4.7(1) μ_B. DFT also gives a C-type magnetic structure with dominant AFM intralayer J_1 interactions and FM interlayer J_2 interactions. Directional magnetic calculations predict that MDD interactions are the strongest directional interaction and that magnetic moments should point along the c axis, in agreement with NPD. However, there is close competition between the slightly stronger MDD interactions and slightly weaker DFT SOC interactions, which prefer moments pointing along the c axis and the $a-b$ plane, respectively. Finally, tetrahedral distortion was measured with NPD, and its effect through crystal-field splitting which was simulated with DFT SOC calculations may be observable in the directional behavior of the magnetic moments in $Ba_2MnSi_2O_7$. On this basis we propose an initial model for the magnetic interactions in $Ba_2MnSi_2O_7$ which consists of SSE, SIA due to crystal-field splitting, and an MDD term.

■ ASSOCIATED CONTENT

Supporting Information

The Supporting Information is available free of charge on the ACS Publications website at DOI: 10.1021/acs.inorgchem.8b03195.

DFT VASP input files (ZIP)

Accession Codes

CCDC 1879121−1879122 contain the supplementary crystallographic data for this paper. These data can be obtained free of charge via www.ccdc.cam.ac.uk/data_request/cif, or by emailing data_request@ccdc.cam.ac.uk, or by contacting The Cambridge Crystallographic Data Centre, 12 Union Road, Cambridge CB2 1EZ, UK; fax: +44 1223 336033.

■ AUTHOR INFORMATION

Corresponding Authors

*E-mail for M.S.: matthew.sale@ansto.gov.au.

*E-mail for M.A.: maxim.avdeev@ansto.gov.au.

ORCID

Matthew Sale: 0000-0001-6492-8084

Maxim Avdeev: 0000-0003-2366-5809

Chris D. Ling: 0000-0003-2205-3106

Notes

The authors declare no competing financial interest.

■ ACKNOWLEDGMENTS

C.D.L. and M.A. received support for this work from the Australian Research Council (DP170100269).

■ REFERENCES

(1) Momma, K.; Izumi, F. VESTA 3 for three-dimensional visualization of crystal, volumetric and morphology data. *J. Appl. Crystallogr.* **2011**, *44*, 1272−1276.

(2) Burzo, E. Sorosilicates. *Condens. Matter* **2005**, *1*, 1.

(3) Smith, J. Reexamination of the crystal structure of melilite. *Am. Mineral.* **1953**, *38*, 643−661.

(4) Swainson, I.; Dove, M.; Schmahl, W.; Putnis, A. Neutron powder diffraction study of the akermanite-gehlenite solid-solution series. *Phys. Chem. Miner.* **1992**, *19*, 185−195.

(5) Röthlisberger, F.; Seifert, F.; Czank, M. Chemical control of the commensurateincommensurate phase transition in synthetic melilites. *Eur. J. Mineral.* **1990**, *2*, 585−594.

(6) Romhányi, J.; Penc, K. Multiboson spin-wave theory for $Ba_2CoGe_2O_7$: A spin-3/2 easyplane Néel antiferromagnet with strong single-ion anisotropy. *Phys. Rev. B: Condens. Matter Mater. Phys.* **2012**, *86*, 174428.

(7) Sale, M.; Avdeev, M.; Mohamed, Z.; Ling, C.; Barpanda, P. Magnetic structure and properties of centrosymmetric twisted-melilite $K_2CoP_2O_7$. *Dalton Trans.* **2017**, *46*, 6409−6416.

(8) Zheludev, A.; Shirane, G.; Sasago, Y.; Koide, N.; Uchinokura, K. Spiral phase and spin waves in the quasi-two-dimensional antiferromagnet $Ba_2CuGe_2O_7$ (vol 54, pg 15163, 1996). *Phys. Rev. B: Condens. Matter Mater. Phys.* **1996**, *54*, 15163.

(9) Endo, T.; Doi, Y.; Hinatsu, Y.; Ohoyama, K. Magnetic and Neutron Diffraction Study on Melilite-Type Oxides $Sr_2MGe_2O_7$ (M = Mn, Co). *Inorg. Chem.* **2012**, *51*, 3572−3578.

(10) Akaki, M.; Yoshizawa, D.; Okutani, A.; Kida, T.; Romhányi, J.; Penc, K.; Hagiwara, M. Direct observation of spin-quadrupolar excitations in $Sr_2CoGe_2O_7$ by high-field electron spin resonance. *Phys. Rev. B: Condens. Matter Mater. Phys.* **2017**, *96*, 214406.

(11) Hutanu, V.; Sazonov, A.; Meven, M.; Roth, G.; Gukasov, A.; Murakawa, H.; Tokura, Y.; Szaller, D.; Bordács, S.; Kézsmárki, I.; Guduru, V.; Peters, L.; Zeitler, U.; Romhányi, J.; Náfrádi, B. Evolution of two-dimensional antiferromagnetism with temperature and magnetic field in multiferroic $Ba_2CoGe_2O_7$. *Phys. Rev. B: Condens. Matter Mater. Phys.* **2014**, *89*, No. 064403.

(12) Kim, J. W.; Khim, S.; Chun, S. H.; Jo, Y.; Balicas, L.; Yi, H.; Cheong, S.-W.; Harrison, N.; Batista, C.; Han, J. H.; Kim, K. H. Manifestation of magnetic quantum fluctuations in the dielectric properties of a multiferroic. *Nat. Commun.* **2014**, *5*, 4419.

(13) Zheludev, A.; Maslov, S.; Shirane, G.; Tsukada, I.; Masuda, T.; Uchinokura, K.; Zaliznyak, I.; Erwin, R.; Regnault, L. Magnetic anisotropy and low-energy spin waves in the Dzyaloshinskii-Moriya spiral magnet $Ba_2CuGe_2O_7$. *Phys. Rev. B: Condens. Matter Mater. Phys.* **1999**, *59*, 11432−11444.

DOI: 10.1021/acs.inorgchem.8b03195
Inorg. Chem. XXXX, XXX, XXX−XXX

(14) Masuda, T.; Kitaoka, S.; Takamizawa, S.; Metoki, N.; Kaneko, K.; Rule, K.; Kiefer, K.; Manaka, H.; Nojiri, H. Instability of magnons in two-dimensional antiferromagnets at high magnetic fields. *Phys. Rev. B: Condens. Matter Mater. Phys.* **2010**, *81*, 100402.
(15) Zheludev, A.; Shirane, G.; Sasago, Y.; Kiode, N.; Uchinokura, K. Spiral phase and spin waves in the quasi-two-dimensional antiferromagnet $Ba_2CuGe_2O_7$. *Phys. Rev. B: Condens. Matter Mater. Phys.* **1996**, *54*, 15163−15170.
(16) Szaller, D.; Bordács, S.; Kézsmárki, I. Symmetry conditions for nonreciprocal light propagation in magnetic crystals. *Phys. Rev. B: Condens. Matter Mater. Phys.* **2013**, *87*, No. 014421.
(17) Perez-Mato, J.; Ribeiro, J. On the symmetry and the signature of atomic mechanisms in multiferroics: the example of $Ba_2CoGe_2O_7$. *Acta Crystallogr., Sect. A: Found. Crystallogr.* **2011**, *67*, 264−268.
(18) Szaller, D.; Bordács, S.; Kocsis, V.; Rõõm, T.; Nagel, U.; Kézsmárki, I. Effect of spin excitations with simultaneous magnetic- and electric-dipole character on the static magnetoelectric properties of multiferroic materials. *Phys. Rev. B: Condens. Matter Mater. Phys.* **2014**, *89*, 184419.
(19) Penc, K.; Romhányi, J.; Rõõm, T.; Nagel, U.; Antal, Á.; Fehér, T.; Jánossy, A.; Engelkamp, H.; Murakawa, H.; Tokura, Y.; Szaller, D.; Bordács, S.; Kézsmárki, I. Spin-stretching modes in anisotropic magnets: spin-wave excitations in the multiferroic $Ba_2CoGe_2O_7$. *Phys. Rev. Lett.* **2012**, *108*, 257203.
(20) Iguchi, Y.; Nii, Y.; Kawano, M.; Murakawa, H.; Hanasaki, N.; Onose, Y. Microwave non-reciprocity of magnon excitations in a non-centrosymmetric antiferromagnet $Ba_2MnGe_2O_7$. *Phys. Rev. B.* **2018**, *98*, No. 064416.
(21) Murakawa, H.; Onose, Y.; Miyahara, S.; Furukawa, N.; Tokura, Y. Comprehensive study of the ferroelectricity induced by the spin-dependent d-p hybridization mechanism in $Ba_2XGe_2O_7$ (X= Mn, Co, and Cu). *Phys. Rev. B: Condens. Matter Mater. Phys.* **2012**, *85*, 174106.
(22) Andrews, K. The lattice parameters and interplanar spacings of some artificially prepared melilites. *Mineral. Mag. J. Mineral. Soc.* **1948**, *28*, 374−379.
(23) Brisi, C. Composti a Struttura Melilitica Ferro e Manganese Bivalenti. *Atti Accad. Sci. Torino* **1961**, *95*, 263.
(24) Ito, J.; Peiser, H. S. Distorted tetrahedra in strontium copper åkermanite. *J. Res. Natl. Bur. Stand., Sect. A* **1969**, *73A*, 69−74.
(25) Gabelica-Robert, M.; Tarte, P. Vibrational spectrum of akermanite-like silicates and germanates. *Spectrochim. Acta, Part A* **1979**, *35*, 649−654.
(26) Kimata, M. The crystal structure of $Sr_2MnSi_2O_7$ melilite. Mineralogy Society of Japan, 1983 Annual Meeting, Abstract A-18, 1983.
(27) Kimata, M. The structural-properties and mineralogical significance of synthetic $Sr_2MnSi_2O_7$ melilite with 4-coordinated manganese. *Neues Jahrb. Mineral., Monatsh.* **1985**, 83−96.
(28) Kiselyova, N. N. Property Prediction for Multicomponent Compounds. Report No. EOARD-SPC-96-4096. European Office of Aerospace Research and Development, 1997.
(29) Golosovsky, I.; Kelberg, E.; Smirnov, O. Crystal and magnetic structures of compounds from melilite group with 3d-ions. *St.-Petersburg Nuclear Physics Institute, Russian Academy Of Sciences* 1998; Preprints, 539.171.018.
(30) Joseph, T.; Sebastian, M. Microwave Dielectric Properties of $(Sr_{1-x}A_x)_2(Zn_{1-x}B_x)Si_2O_7$ Ceramics (A = Ca, Ba and B = Co, Mg, Mn, Ni). *J. Am. Ceram. Soc.* **2010**, *93*, 147−154.
(31) Endo, T.; Doi, Y.; Wakeshima, M.; Hinatsu, Y. Crystal Structures and Magnetic Properties of New Europium Melilites $Eu_2MSi_2O_7$ (M = Mg, Mn) and Their Strontium Analogues. *Inorg. Chem.* **2010**, *49*, 10809−10814.
(32) Koo, H. On the long-range magnetic order and the preferred spin orientation of the layered magnetic oxides $Sr_2MnSi_2O_7$ and $Ba_2MnGe_2O_7$. *Solid State Commun.* **2012**, *152*, 1116−1118.
(33) Akaki, M.; Tadokoro, T.; Kuwahara, H.; Kihara, T.; Tokunaga, M. Anisotropic magnetic properties in Åkermanite $Sr_2MSi_2O_7$ (M = Co, Mn) crystals. *J. Korean Phys. Soc.* **2013**, *62*, 1812−1814.
(34) Yoshida, T.; Soda, M.; Hagihala, M.; Hayashida, S.; Masuda, T. Magnetic properties of two-dimensional square-lattice antiferromagnets $Sr_2MSi_2O_7$ (M = Cu, Co, Mn). *Meeting Abstracts of the Physical Society of Japan* **2016**, *71.1*, 19aPS−51.
(35) Materials Project mp-25703 $Sr_2MnGe_2O_7$; https://materialsproject.org/materials/mp-25703/.
(36) Naruse, H. Synthesis and crystal structure of $Sr_2MnGe_2O_7$. *Rep. Res. Lab. Eng. Mater., Tokyo Inst. Technol.* **1984**, 1−9.
(37) Koo, H.; Lee, C.; Whangbo, M. Density functional analysis of the magnetic structures of $Sr_2MGe_2O_7$ (M = Mn, Co). *J. Magn. Magn. Mater.* **2012**, *324*, 3716−3718.
(38) Kim, T.; Kim, S.; Lin, C.; Liu, R.; Chan, T.; Im, S. Melilite-type blue chromophores based on Mn3+ in a trigonal-bipyramidal coordination induced by interstitial oxygen. *J. Mater. Chem. C* **2013**, *1*, 5843−5848.
(39) Su, J.; Guo, Y.; Zhang, J.; Sun, H.; He, J.; Lu, X.; Lu, C.; Zhu, J. Study on optical, dielectric, and magnetic properties of $Ba_2MnGe_2O_7$ ceramics. *Proceedings of ISAFECAPD-PFM 2012, Aveiro* **2012**, *2012*, 1−3.
(40) Granata, V.; Ubaldini, A.; Fittipaldi, R.; Rocco, L.; Pace, S.; Vecchione, A. Synthesis and characterization of mixed melilite-type oxides. *J. Cryst. Growth* **2017**, *457*, 128−131.
(41) Sazonov, A.; Hutanu, V.; Meven, M.; Roth, G.; Georgii, R.; Masuda, T.; Nafradi, B. Crystal Structure of Magnetoelectric $Ba_2MnGe_2O_7$ at Room and Low Temperatures by Neutron Diffraction. *Inorg. Chem.* **2018**, *57*, 5089−5095.
(42) Iguchi, Y.; Nii, Y.; Kawano, M.; Murakawa, H.; Hanasaki, N.; Onose, Y. Microwave nonreciprocity of magnon excitations in the noncentrosymmetric antiferromagnet $Ba_2MnGe_2O_7$. *Phys. Rev. B: Condens. Matter Mater. Phys.* **2018**, *98*, No. 064416.
(43) Endo, T.; Doi, Y.; Wakeshima, M.; Suzuki, K.; Matsuo, Y.; Tezuka, K.; Ohtsuki, T.; Shan, Y. J.; Hinatsu, Y. Magnetic Properties of the Melilite-Type Oxysulfide $Sr_2MnGe_2S_6O$: Magnetic Interactions Enhanced by Anion Substitution. *Inorg. Chem.* **2017**, *56*, 2459−2466.
(44) Stober, S.; Pollmann, H. Phase Assemblages in the System $Ca_2Al_2SiO_7$ - "$Ca_2MnSi_2O_7$" Related to a Modified CAC Clinker. *Appl. Mineral.* **2004**, 321−324.
(45) Redhammer, G. J.; Roth, G.; Amthauer, G.; Lottermoser, W. On the crystal chemistry of olivine-type germanate compounds, $Ca_{1+x}M_{1-x}GeO_4$ (M2+ = Ca, Mg, Co, Mn). *Acta Crystallogr., Sect. B: Struct. Sci.* **2008**, *64*, 261−271.
(46) Kimata, M. Crystallo-chemical evolution of a crystal structure due to cationic substitution after the example of melilite. *Naturwissenschaften* **1985**, *72*, 372−373.
(47) Kimata, M. The crystal-structure of manganoan kilchoanite, $Ca_{2.33}Mn_{0.67}Si_2O_7$ − A site-preference rule for the substitution of Mn for Ca. *Mineral. Mag.* **1989**, *53*, 625−631.
(48) Xia, Q. Private communication. Our own attempts to synthesize pure melilite $Ca_2MnSi_2O_7$ and $Ca_2MnGe_2O_7$ were also unsuccessful, resulting in a glasslike material and various crystalline materials, respectively.
(49) Brisi, C.; Abbattista, F. Melilites. IV. Germanium compounds with a melilitic structure. *Ann. Chim. (Rome, Italy)* **1960**, *50*, 1786−1790.
(50) Kimata, M. Synthetic Mn-kilchoanite - A new development in polymorphism of melilite. *Mineral. Mag.* **1986**, *50*, 511−515.
(51) Iishi, K.; Fujimoto, K.; Fujino, K. Single-crystal growth of akermanites $Ca_2Mg_{1-x}Co_xSi_2O_7$ with modulated structure. *Neues Jahrb. Mineral., Monatsh.* **1989**, 219−226.
(52) Skomski, R. *Simple models of magnetism*; Oxford University Press on Demand, 2008.
(53) JCPDS No. 00-039-0264.
(54) Avdeev, M.; Xia, Q.; Sale, M.; Allison, M.; Ling, C. Crystal structure and monoclinic distortion of glaserite-type $Ba_3MnSi_2O_8$. *J. Solid State Chem.* **2018**, *266*, 1−8.
(55) Savitzky, A.; Golay, M. J. E. Smoothing and Differentiation of Data by Simplified Least Squares Procedures. *Anal. Chem.* **1964**, *36*, 1627−1639.

DOI: 10.1021/acs.inorgchem.8b03195
Inorg. Chem. XXXX, XXX, XXX−XXX

(56) Avdeev, M.; Hester, J. R. ECHIDNA: a decade of high-resolution neutron powder diffraction at OPAL. *J. Appl. Crystallogr.* **2018**, *51*, 1597.
(57) Rodríguez-Carvajal, J. Recent advances in magnetic structure determination by neutron powder diffraction. *Phys. B* **1993**, *192*, 55−69.
(58) Kresse, G.; Hafner, J. Ab initio molecular-dynamics simulation of the liquid-metalamorphous-semiconductor transition in germanium. *Phys. Rev. B: Condens. Matter Mater. Phys.* **1994**, *49*, 14251.
(59) Kresse, G.; Hafner, J. Abinitio molecular-dynamics for liquid-metals. *Phys. Rev. B: Condens. Matter Mater. Phys.* **1993**, *47*, 558−561.
(60) Kresse, G.; Furthmuller, J. Efficiency of ab-initio total energy calculations for metals and semiconductors using a plane-wave basis set. *Comput. Mater. Sci.* **1996**, *6*, 15−50.
(61) Kresse, G.; Furthmuller, J. Efficient iterative schemes for ab initio total-energy calculations using a plane-wave basis set. *Phys. Rev. B: Condens. Matter Mater. Phys.* **1996**, *54*, 11169−11186.
(62) Perdew, J. P.; Burke, K.; Ernzerhof, M. Generalized gradient approximation made simple. *Phys. Rev. Lett.* **1996**, *77*, 3865.
(63) Blöchl, P. E. Projector augmented-wave method. *Phys. Rev. B: Condens. Matter Mater. Phys.* **1994**, *50*, 17953.
(64) Kresse, G.; Joubert, D. From ultrasoft pseudopotentials to the projector augmentedwave method. *Phys. Rev. B: Condens. Matter Mater. Phys.* **1999**, *59*, 1758−1775.
(65) Monkhorst, H. J.; Pack, J. D. Special points for Brillouin-zone integrations. *Phys. Rev. B* **1976**, *13*, 5188.
(66) Fu, C.; Ho, K. First-principles calculation of the equilibrium ground-state properties of transition metals: Applications to Nb and Mo. *Phys. Rev. B: Condens. Matter Mater. Phys.* **1983**, *28*, 5480.
(67) Dudarev, S.; Botton, G.; Savrasov, S.; Humphreys, C.; Sutton, A. Electron-energy-loss spectra and the structural stability of nickel oxide: An LSDA+U study. *Phys. Rev. B: Condens. Matter Mater. Phys.* **1998**, *57*, 1505−1509.
(68) Wang, L.; Maxisch, T.; Ceder, G. Oxidation energies of transition metal oxides within the GGA+U framework. *Phys. Rev. B: Condens. Matter Mater. Phys.* **2006**, *73* (19), 195107.
(69) Floris, A.; de Gironcoli, S.; Gross, E.; Cococcioni, M. Vibrational properties of MnO and NiO from DFT+U-based density functional perturbation theory. *Phys. Rev. B: Condens. Matter Mater. Phys.* **2011**, *84*, 161102.
(70) Franchini, C.; Bayer, V.; Podloucky, R.; Paier, J.; Kresse, G. Density functional theory study of MnO by a hybrid functional approach. *Phys. Rev. B: Condens. Matter Mater. Phys.* **2005**, *72*, No. 045132.
(71) Francis, G.; Payne, M. Finite basis set corrections to total energy pseudopotential calculations. *J. Phys.: Condens. Matter* **1990**, *2* (19), 4395.
(72) Xiang, H.; Lee, C.; Koo, H.; Gong, X.; Whangbo, M. Magnetic properties and energymapping analysis. *Dalton Trans.* **2013**, *42* (4), 823−853.
(73) Liechtenstein, A. I.; Anisimov, V. I.; Zaanen, J. Density-functional theory and strong interactions: Orbital ordering in Mott-Hubbard insulators. *Phys. Rev. B: Condens. Matter Mater. Phys.* **1995**, *52*, R5467−R5470.
(74) Bousquet, E.; Spaldin, N. J dependence in the LSDA+U treatment of noncollinear magnets. *Phys. Rev. B: Condens. Matter Mater. Phys.* **2010**, *82*, 220402.
(75) Xu, D.; Sale, M.; Avdeev, M.; Ling, C. D.; Battle, P. D. Experimental and computational study of the magnetic properties of $ZrMn_{2-x}Co_xGe_4O_{12}$. *Dalton Trans.* **2017**, *46*, 6921−6933.
(76) Koo, H.-J.; Xiang, H.; Lee, C.; Whangbo, M.-H. Effect of magnetic dipole-dipole interactions on the spin orientation and magnetic ordering of the spin-ladder compound $Sr_3Fe_2O_5$. *Inorg. Chem.* **2009**, *48*, 9051−9053.
(77) den Hertog, B. C.; Gingras, M. J. Dipolar interactions and origin of spin ice in Ising pyrochlore magnets. *Phys. Rev. Lett.* **2000**, *84*, 3430.
(78) Koo, H.-J.; Whangbo, M.-H. Spin Exchange and Magnetic Dipole−Dipole Interactions Leading to the Magnetic Superstructures of MAs_2O_6 (M= Mn, Co, Ni). *Inorg. Chem.* **2014**, *53*, 3812−3817.
(79) Tackett, R.; Parsons, J.; Machado, B.; Gaytan, S.; Murr, L.; Botez, C. Evidence of lowtemperature superparamagnetism in Mn_3O_4 nanoparticle ensembles. *Nanotechnology* **2010**, *21*, 365703.
(80) Reynaud, M.; Rousse, G.; Chotard, J.-N.; Rodríguez-Carvajal, J.; Tarascon, J.-M. Marinite $Li_2M(SO_4)_2$ (M = Co, Fe, Mn) and $Li1Fe(SO_4)_2$: Model Compounds for Super-Super-Exchange Magnetic Interactions. *Inorg. Chem.* **2013**, *52*, 10456−10466 PMID: 23978225 .
(81) Figgis, B.; Lewis, J. *Modern Coordination chemistry, Principles and Methods*; Lewis, J., Wilkinsone, R. J., Eds.; Interscience: New York, 1968; p 403.
(82) Kuo, Y.-K.; Figueroa, E.; Brill, J. Mean-field specific heat of $CuGeO_3$. *Solid State Commun.* **1995**, *94*, 385−389.
(83) Chung, M.; Kuo, Y.-K.; Mozurkewich, G.; Figueroa, E.; Teweldemedhin, Z.; Di Carlo, D.; Greenblatt, M.; Brill, J. Specific heat at CDW transitions in bronzes. *J. Phys. IV* **1993**, *03*, C2-247.
(84) Melzi, R.; Aldrovandi, S.; Tedoldi, F.; Carretta, P.; Millet, P.; Mila, F. Magnetic and thermodynamic properties of Li_2VOSiO_4: A two-dimensional S= 1/2 frustrated antiferromagnet on a square lattice. *Phys. Rev. B: Condens. Matter Mater. Phys.* **2001**, *64*, No. 024409.
(85) Kayser, P.; Martínez-Lope, M. J.; Retuerto, M.; Sánchez-Benítez, J.; Fernández-Díaz, M. T.; Alonso, J. A. Correlation between the crystal structure and the Curie temperature in $RCu_3(Mn_3Fe)O_{12}$ (R= rare-earth) complex perovskites. *Dalton Trans.* **2012**, *41*, 10670−10679.
(86) Jo, Y.; Park, J.-G.; Kim, H.; Ratcliff, I.; Cheong, S. Pressure-dependent magnetic properties of geometrically frustrated $ZnCr_2O_4$. *Phys. Rev. B: Condens. Matter Mater. Phys.* **2005**, *72*, 184421.
(87) Fisher, M. E. Relation between the specific heat and susceptibility of an antiferromagnet. *Philos. Mag.* **1962**, *7*, 1731−1743.
(88) Opechowski, W. T.; Guccione, R. *Magnetism*; Rado, G. T., Suhl, H., Eds.; Academic Press: New York, Vol. II, Part A, 1965.
(89) Robinson, K.; Gibbs, G.; Ribbe, P. Quadratic elongation: a quantitative measure of distortion in coordination polyhedra. *Science* **1971**, *172*, 567−570.
(90) Companion, A.; Komarynsky, M. Crystal field splitting diagrams. *J. Chem. Educ.* **1964**, *41*, 257.
(91) Orgel, L. E. *An Introduction to Transition-metal Chemistry: Ligand-field Theory*; Taylor & Francis: 1966.

DOI: 10.1021/acs.inorgchem.8b03195
Inorg. Chem. XXXX, XXX, XXX−XXX